Lab on a Chip

A micro-scale rheometer to study foam texture and flow resistance in planar fractures

Journal:	*Lab on a Chip*
Manuscript ID	LC-ART-07-2022-000595
Article Type:	Paper
Date Submitted by the Author:	01-Jul-2022
Complete List of Authors:	Nazari, Negar; Stanford University, Energy Resources Engineering Kovscek, A.; Stanford University, Energy Resources Engineering

SCHOLARONE™
Manuscripts

Journal Name

A micro-scale rheometer to study foam texture and flow resistance in planar fractures [†]

Negar Nazari[a], and Anthony R. Kovscek[*a]

We designed and fabricated a new microfluidic device to better enable study of foam microstructure and rheology in planar fractures. The design phase included stress-strain finite element analysis to enhance the pressure tolerance of the device. The optimized design is a 2-cm wide by 7.75-cm long rough fracture that includes 25 posts to anchor the glass cover plate. The posts simulate asperities and provide structural support during bonding of a glass cover plate to the device. Importantly, the new design illustrates improved ability to sustain large differential pressure compared to previous designs in the literature. The rheometer permits study of the relationship among foam bubble morphology, pressure drop, and flow rates. Our findings validated the previous, sparse microvisual studies mentioned in the literature and confirmed that small quality foam, ranging from 20 to 50% gas by volume, contains dispersed bubbles separated by liquid lenses. In this range, the distribution of bubble sizes was roughly 80-90% small uniform bubbles and only 10-20% of larger and more elongated bubbles. Additionally, our studies reveal that foam apparent viscosity is a strong function of foam quality, velocity, and texture (i.e., bubble size). Apparent viscosity of foam ranged from 100 to 600 cP for the conditions studied. High quality foams in fractures are independent of gas flow rates but very sensitive to liquid flow rates. On the other hand, low quality foams are sensitive to gas flow rates but independent of liquid flow rates.

1 Introduction

Foam is a colloidal dispersion consisting of a gas, a liquid, and a liquid-soluble foaming agent[1,2]. Gas bubbles are dispersed in the continuous liquid phase and they are separated by thin liquid films called lamella[3]. Foaming a gas within a porous medium is an effective method to increase the flow resistance of the gas and thereby alleviate challenges faced during subsurface remediation processes and to assist in the storage of carbon dioxide in saline formations[4].

Fractured porous media have complicated topology that results in complex single and multiphase flows. The permeability contrast between fractures and matrix contributes to this complexity. One option, to improve the fluid transport efficiency through fractures and increase the recovery of non-aqueous phase liquids for aquifer remediation, is to reduce the gas mobility by foaming the injectant[5–13]. Foam provides mobility control in fractures and systems featuring large permeability contrasts[14–17].

Accurate and detailed understanding of foam physics contributes to successful use of foam for aquifer remediation, improved hydrocarbon recovery efficiency, and hydraulic fracturing[18]. Macroscopic properties of foam such as viscous pressure drop and displacement efficiency depend on microscopic properties (foam texture) and processes controlling foam generation and coalescence. Magnetic resonance imaging (MRI) and computed tomography (CT) enable in-situ imaging at core scale; however, they do not yield sufficient pore-scale spatial resolution required for visualizing lamella creation, coalescence and transport[18].

The literature review to follow documents the fundamental importance of visualizing the microstructure of foam within fractures in conjunction with complex flow resistance trends. Additionally, this review reveals gaps in mechanistic understanding of the interplay of bubble texture, fluid flow rates, and gas mobility that are addressed with simultaneous measurements of flow resistance and bubble morphology using microfluidic devices. Accordingly, this work reports a novel, visual foam rheometer to quantify foam texture and flow resistance. This new design is suitable for both probing flow behavior specifically in fractures and observing details of the complex fluid micro structure. Results and discussion round out the paper.

2 Foam in Fractures

Different apparatus have been used extensively to study foam flow behavior in fractures. Transparent epoxy replicas[17], etched

[a] Stanford University, Energy Sciences and Engineering, 367 Panama St, room 50, Stanford, California, USA. E-mail: kovscek@stanford.edu

‡ Additional footnotes to the title and authors can be included *e.g.* 'Present address:' or 'These authors contributed equally to this work' as above using the symbols: ‡, §, and ¶. Please place the appropriate symbol next to the author's name and include a \footnotetext entry in the the correct place in the list.

silicon wafers[15,19], glass plates[20,21], marble tiles[22], acrylic plates[23,24], and replicas of real rocks[25] are examples. Many foam flow in fracture experiments were conducted under atmospheric pressure conditions[17,20,23] and few studies have been conducted at slightly elevated pressures[15,19].

Foam exhibits large flow resistance and unusual rheological properties in unfractured porous media[22,26–29]. Similarly, foam fluid rheology in fractured media depends on the shape and size of the bubbles. Changes in flow behavior are directly related to the transformation of the bubble morphology[17]. Foam-generation mechanisms in fractures are a function of aperture and roughness length scale, fracture-wall geometry, gas fractional flow, and total superficial velocity[21]. Pancharoen et al.[7] found similar underlying physics for foam generation and coalescence and flow resistance, in both fractured and unfractured media. Buchgraber et al.[15] found that adding roughness increased the number of foam germination sites leading to more snap-off. AlQuaimi and Rossen observed in-situ foam generation in fractures as a result of snap-off and lamellae division.

The morphology of foam is characterized by the volume fraction of gas, or quality, in the generated foam. At high gas volume fractions, or dry foams, the continuous liquid phase presents in the thin films between polyhedral bubbles and in the plateau borders. However, in wet foams, the spherical gas bubbles are well dispersed in the continuous phase. Depending on the stabilization mechanism, gas and liquid types, and preparation techniques, the foam bubbles can be monodisperse or polydisperse. Princen[30] predicted that a transition happens in foam bubble shape from polyhedral to spherical at the gas fraction of 0.9069 in two-dimensional geometries. Kovscek at al.[17] observed a similar transition in rough fractures at a foam quality of 92%. During the transition to wetter foams, the radius of interfacial curvature increases and the pressure gradient decreases[17,31]. Buchgraber et al.[15] showed that foam at small qualities, ranging from 20 to 60%, contains sparsely dispersed bubbles in liquid, that consisted roughly of 90% small uniform bubbles and 10% of large elongated bubbles.

Considering the sensitivity of flow resistance and pressure gradient with respect to liquid and gas phases, two different foam flow regimes in fractures are defined. Within the low quality regime that was found to range from gas fractional flows of about 20 to 70%, pressure gradient is sensitive to the rate of injection of the gaseous phase and independent of the rate injection of the gaseous phase[15]. However, in the high quality regime, pressure gradient is sensitive to the rate of injection of the liquid phase and less sensitive to the rate of injection of the gaseous phase[15,17,21].

Increasing liquid rate results in creation of smaller bubbles[27]. The foam apparent viscosity increases as a result of increasing foam texture[20]. As a result, the pressure gradient and flow resistance increases. However, increasing gas flow rate results in greater lamellae coalescence and larger bubbles[31]. Several studies[15,22–25] showed that increasing foam quality corresponds to increasing size and stability of the bubbles and pressure gradient up to a critical foam quality and thereafter, foam coalescence happens. Capillary-suction coalescence of foam lamellae becomes significant when the local aqueous phase saturation is very low[22].

Under the condition of high foam quality, the generated foam bursts quickly, resulting in a decrease in the proportion of bubbles that can effectively seal the fractures during the flow process, and so the pressure drop decreases. Surfactant-solution type and concentration are also important to coalescence.

A study by Pancharoen et al.[7] investigated foam flow in a linear fracture in which the aperture varies along the fracture length. They showed that the fracture aperture plays an important role in foam-flow characterization. During foam flow in a variable-thickness fracture, in addition to the smooth fracture wall influencing the foam viscosity, the Jamin effect caused by foam deformation is a significant contributor to the flow resistance[23]. Alquaimi and Rossen[21] used variable aperture fracture models to investigate the effect of fracture aperture on foam trapping. They observed noticeable foam trapping in fractures with apertures of less than 50 μm. Li and Rossen[32] confirmed that by increasing the interstitial velocity and pressure gradient, gas trapping decreased and foam texture becomes finer. In rough-walled fractures, foam propagation through permeable paths produces strong flow resistance[15].

The literature above reveals gaps in mechanistic understanding of the interplay of bubble texture, fluid flow rates, and gas mobility that are addressed with simultaneous measurements of flow resistance and bubble morphology. Several researchers reviewed microfluidic viscometers for studying shear rheology of complex fluids and biofluids[33–35]. The studies are based on the conventional methods of measuring rheological properties such as the relationship between the shear stress and shear rate. They speak to the importance of microfluidic rheometry and detail advantages over conventional measurements. Clearly, microfluidics for rheological studies assists in better understanding of complex fluids and uncovers structure-property relations. Additionally, we can develop constitutive models[19] and unravel the fundamental mechanisms that regulate fluid movement. Accordingly, we developed a novel foam rheometer based on microfluidic principles to quantify foam texture and flow resistance.

3 Methodology

The design process to optimise the mechanical performance of a silcon-glass composite microfluidic device and the subsequent fabrication process are discussed next.

3.1 Design Optimization

Microscale observations using silicon-based micromodels are extensive for studying multiphase flow properties and fluid-fluid interactions[19,32,36,37]. An instrumented micromodel is useful to visualize the microscopic flow of foam in fractures. This instrument enables pressure drop measurements and foam microstructure observations for a wide range of flow rates and foam qualities. To conduct our experiments, we required a new micromodel that is capable of withstanding greater pressure gradients than previous designs. Therefore, we prepared an optimized design of a planar fracture to withstand relatively high-pressure conditions.

We employed SOLIDWORKS to conduct stress, strain, and displacement analysis using finite element methods. Applying this

strategy helped us to evaluate model mechanical response over a wide range of pressure differences between the inside and outside of the micromodel. Figure 1 shows our base and final, optimized planar fracture designs.

The design optimization process begins from an earlier planar fracture by ref.[15]. This previous design was not capable of tolerating pressure drops greater than 138 kPa. The steps to increase the maximum pressure tolerance of the rheometer were

- modify the design of the boundary to eliminate sharp corners by replacing sharp edges and corners with curved lines because they do not have stress accumulation points,

- change the cross-sectional shape of internal support features from square to circular cross section,

- progressively increase the number of internal support features, and

- increase the diameter of internal support features.

Following each of the steps above, the stress, strain, and displacement of the micromodel was calculated under a 690 kPa differential pressure. The third and fourth steps were repeated until the strain was less than 2×10^{-5}.

The finite element equations solved for the element equilibrium equation and problem formulation are[38]

$$[k]\{q\} = \{p\} \tag{1}$$

where $\{q\}$ is nodal displacements vector and $\{p\}$ is the force vector (volume and surface loads) defined as

$$\{p\} = \int_V [N]^T \{P^V\} dV + \int_S [N]^T \{P^S\} dS \tag{2}$$

Any thermal effects are neglected. The stiffness matrix $[k]$ is defined as

$$[k] = \int_v [B]^T [E][B] dV \tag{3}$$

where $[B]$ is the displacement differentiation matrix and $[E]$ is the elasticity matrix

$$[E] = \begin{bmatrix} \lambda+2\mu & \lambda & \lambda & 0 & 0 & 0 \\ \lambda & \lambda+2\mu & \lambda & 0 & 0 & 0 \\ \lambda & \lambda & \lambda+2\mu & 0 & 0 & 0 \\ 0 & 0 & 0 & \mu & 0 & 0 \\ 0 & 0 & 0 & 0 & \mu & 0 \\ 0 & 0 & 0 & 0 & 0 & \mu \end{bmatrix} \tag{4}$$

Here, λ and μ are elastic Lame constants that are expressed through the Young's modulus, E, and Poisson ratio, ν, as

$$\lambda = \frac{\nu E}{(1+\nu)(1-2\nu)} \tag{5}$$

$$\mu = \frac{E}{2(1+\nu)} \tag{6}$$

Strains inside an element are determined with the use of the displacement differentiation matrix that is written as

$$\{\varepsilon\} = [B]\{q\} \tag{7}$$

Stresses are calculated using Hook's law according to

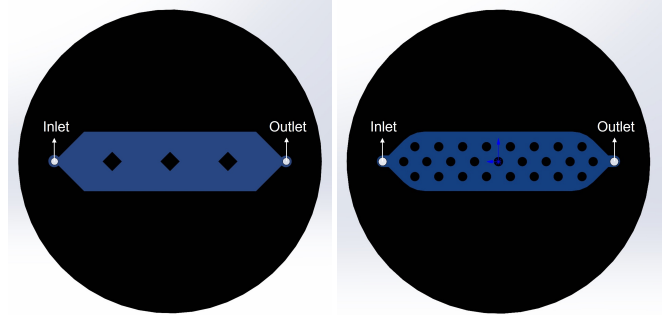$$\{\sigma\} = [E](\{\varepsilon\} - \{\varepsilon^t\}) \tag{8}$$

Fig. 1 Left: The initial micromodel design with its inlet and outlet ports. Right: The optimal micromodel design with its inlet and outlet ports. Blue represents etched area while black is area available to bond the glass coverplate to the silicon wafer.
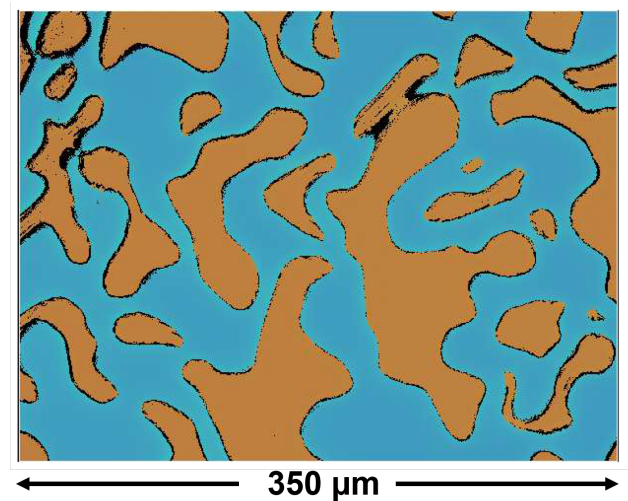

350 µm

25 ± 1µm

12 ± 2µm

Fig. 2 Top: The sandstone-like pattern printed and etched on the wafer to create the fracture roughness. The x-length of the pattern is 350 µm. Bottom: The topography of the etching of the fracture aperture and the side view of the fracture roughness.

3.2 Micromodel Fabrication

We fabricated the etched-silicon micromodels at the Stanford Nanofabrication Facility (SNF). Further details about the instruments and procedures are found at `https://snfexfab.stanford.edu`. K-prime silicon wafers were purchased from WRS Materials. Their thickness and diameter are 500-550 μm and 100 $\pm$ 0.5 mm, respectively. Wafers were dehydrated in a prime YES (Yield Engineering Systems) oven at 150 $^\circ C$ for 30 minutes using hexamethyldisilazane (HMDS) to establish better coverage and adhesion between oxides and resists. Next, we coated the primed wafers with Shipley 3612 photoresist using the SVG (Silicon Valley Group) coater and an automated track system for dispensing 1.6 μm-thick photoresist on 4" silicon wafers [39,40]. Then, we employed a Heidelberg MLA-150, (maskless system) to print on the wafers.

Blank silicon wafers underwent direct-write lithography in the Heidelberg at a wavelength of 405 nm for the light source, a dose of 95 mJ/cm^2, and defoc value of -2. Following that, the wafers were processed through the SVG developer and post-baked to expose photoresist. The wafers were developed for 1 minute using MF-26A developer and post-baked at 110 $^\circ C$ for 120 seconds. Then, the wafers were ready for etching.

Two steps of etching were conducted. In the first run, wafers were etched 25 $\pm$ 1 μm using an Inductive Charged Plasma Deep Reactive Ion etcher with the etching rate of 3 μm/min. Then, the remaining photoresist on the wafers was removed by soaking the wafers in a chemical bath of "piranha" (90% sulfuric acid/hydrogen peroxide) for 20 minutes and at the temperature of 120 $^\circ C$. After washing the wafers, they were dried in a spin-dryer. Then, wafers were baked and coated a second time using the YES oven and SVG coater, respectively. In this stage, the Karl Suss MA-6 Contact Aligner system was employed to perform precision mask-to-wafer back-side alignment and near-UV photoresist exposure on the prepared wafer for 1.6 s. A soft-contact configuration and alignment gap of 40 μm were also employed.

A sandstone pattern with 46% porosity was then etched on the base of the fracture to generate surface roughness. The size of the asperities varies between 30 to 300 μm. Figure 2 depicts the design used to create the fracture roughness. The printed matrix of roughness has 12 $\pm$ 2 μm depth and covers the entire area of the fracture. Figure 2 shows the cross-section of the design after etching.

Thereafter, we used a 0.75 μm-diameter diamond-coated drill bit to perforate the wafer and create two ports for fluid injection and production. Figure 1 shows the initial and final micromodel designs and location of the ports and islands. Then, the remaining photoresist and the small silicon shreds on the wafers was removed by soaking the wafers in "piranha" for another 20 minutes at the temperature of 120 $^\circ C$.

Finally, we bonded an optically flat borofloat glass (Howard Glass) wafer to the top of a clean wafer using an in-house anodic bonding setup at 1045 V and 300 $^\circ C$ for 1 hour [39,40]. Surfaces are water wet due to the formation of an oxide layer during bonding. Micromodels are used in the water-wet state. Prepared micromodels were placed inside a holder prior to experiments.

4 Experimental Procedure

Figure 3 is a schematic of the experimental apparatus. We inject nitrogen gas and foamer solution simultaneously and measure flow parameters. We prepared the foamer solution by dissolving Bioterg Alpha olefin Sulfonate (AS-40) surfactant in 0.5 wt.% NaCl brine solution. The final concentration of the surfactant in the brine was 0.5 wt.%. The AOS was from Stepan and the NaCl was purchased from Thermo Fisher Chemicals Inc. The brine was prepared by dissolving NaCl in house deionized water followed by addition of surfactant.

We controlled the nitrogen injection using a mass flow controller (Bronkhorst EL-FLOW Select) while the liquid injection was controlled by a syringe pump (Harvard). Foam quality was obtained by measuring the injected gas and liquid volumes. The rates of injection were chosen to achieve the desired foam qualities. We apply back pressure while injecting foam to reduce the superficial velocity in the fracture. Back pressures ranged from 135.8 kPa to 342.7 kPa with the increment of 34.5 kPa. The gas flow rates ranged from 4.02 μL/min to 10.15 μL/min that corresponds to 11.6 m/day to 29.2 m/day. The limiting factor to achieve smaller rates of injection is the limited flow rate range of the gas flow controller to provide a larger quality spectrum. Foamer solution rate was chosen to achieve foam qualities that ranged from 20% to 99%. The gas rate was kept constant, generally, and the liquid rate was changed accordingly to obtain a set of data.

Foam is pregenerated by injecting the surfactant laden brine and N_2 through a sandpack (100-200 mesh). Pregenerated foam was then injected through the linear fracture that was initially saturated with water and allowed to come to steady state. Thereafter, we investigated pressure gradient and foam viscosity for various foam qualities and water velocities along the length of the fracture for all different experiments.

A "Z16APO"-model microscope (Leica) microscope with a photo tube that connects to a video camera was employed to visualize the flow pattern at the pore-level in the micromodel. Macroscopic images and videos showing foam quality and texture were captured and analyzed to calculate the bubble texture and the aqueous phase saturation along the micromodel. Simultaneously, we measured the pressure drop across the micromodel during the entire experiment (QuickStart^{TM} M6 Pressure Sensor Evaluation Kit (I2CPS200M6 $EVAL$) IDEX Health & Science, LLC). The sensitivity of the pressure sensors is 0.021 kPa (0.003 psi).

5 Results and Discussion

5.1 Design Optimization

Injecting foam into the planar fracture microfluidic device requires back pressure in order to compress the gas and reduce the velocities to be closer to field conditions. In the absence of design optimization, the minimum gas velocity that we can achieve is around 30 m/day. The optimized design is a fracture with a width and length of 2 and 7.75 cm, respectively. It includes 25 posts to anchor the glass cover plate and provide more structural support during bonding. The depth of the fracture is 25 $\pm$ 1 μm. The calculated porosity of the fracture for the initial and the final
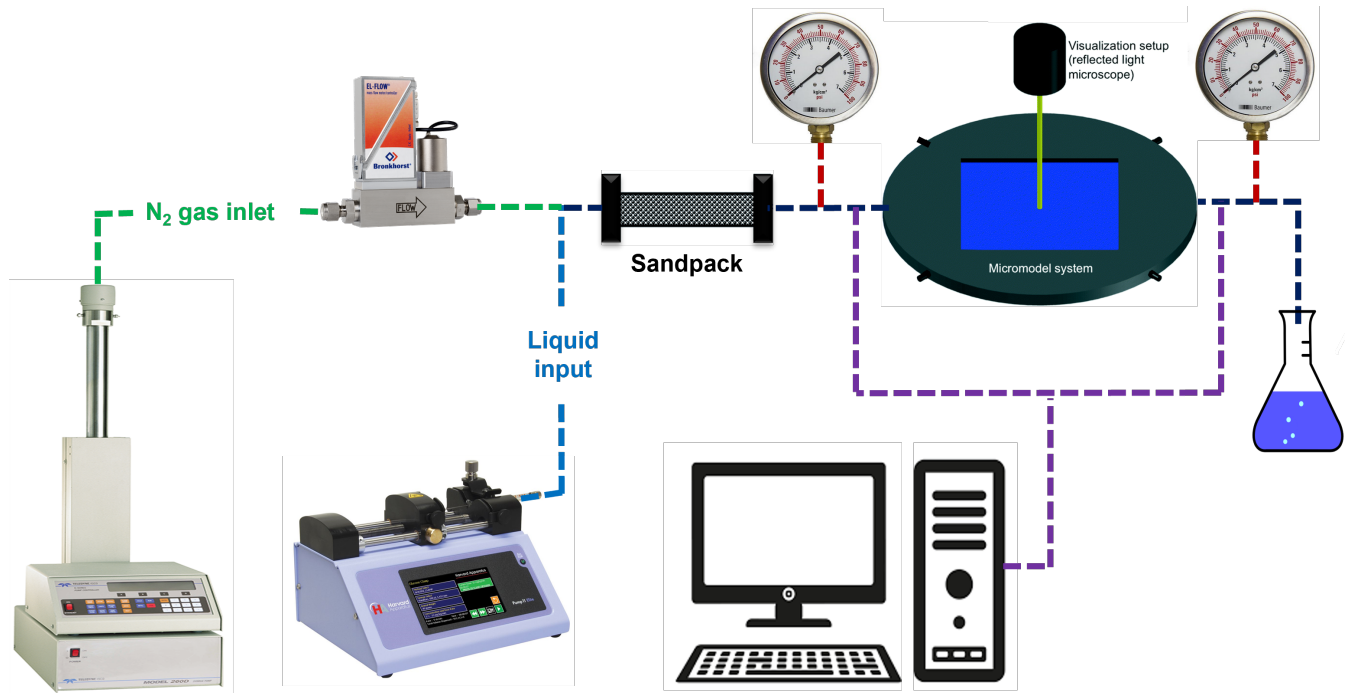
Fig. 3 Schematic of the experimental setup.

designs are 81.3 and 73.6%, respectively.

Analyzing the results in Fig. 4 for the initial design shows that the stress accumulation points fall on the boundaries, especially along the sharp edges and corners, and the areas with minimum bonding support. Therefore, changing the boundary geometry and adding more grains to simulate asperities in the fracture plane and support the bonding of a coverplate to the micromodel improves the pressure tolerance of the design. Additionally, increasing the diameter of the round grains assists in improving the pressure the device can withstand.

Figure 4 also compares side by side the stress, strain, and displacement distribution across the initial and final fracture designs. The left figures show the stress, strain, and displacement distributions for the initial micromodel design including a planar fracture with three square islands with 3-mm side sizes. The right figures show the same distributions for the final micromodel design with optimized round grains that are 3-mm diameter.

Table 1 lists the finite element analysis results for the old and new micromodel designs. Comparing the stress values shows that increasing the number of islands and eliminating the sharp edges decreases the maximum stress encountered from 5502 kPa to 1034 kPa. This also results in decreasing the strain from 5.21 $\times 10^{-5}$ to 1.10 $\times 10^{-5}$ and displacement values from 1.810 to 0.063 μm. Hence, changing the design corresponds to reducing the stress, strain, and displacement by 5 to 6 times. The new micromodel design withstands at least 690 kPa differential pressure enabling significantly smaller superficial gas velocities and experimental conditions closer to the field.

Table 1 The finite element analysis results for the two micromodel designs.

	Initial design	Final design
Number of islands	3	25
Islands' diameter (mm)	3	3
Porosity (%)	98.0	86.9
Maximum stress (kPa)	5502	1034
Maximum displacement (μm)	1.81	0.063
Maximum strain	5.21E-05	1.10E-05

5.2 Validation

To validate measurements from our linear fracture microfluidic rheometer, we first calculated the apparent viscosity of foam from experiments assuming plane Poiseuille flow as

$$\mu_{app} = \frac{|\Delta P| b^2 Q_f}{12 L u_g} \tag{9}$$

where ΔP is the pressure drop, L is the length of the fracture, Q_f is foam quality, u_g is the gas superficial velocity, and b is the fracture aperture. To be clear, u_g/Q_f is the superficial velocity of the foam, v_f.

Next, we use a classical model describing foam viscosity as explained in [19]

$$\mu_f = \mu_g + \frac{\alpha n_f}{v_f^{1/3}} \tag{10}$$

where μ_g is the gas viscosity in the absence of foam and α is a constant that is a function of gas-liquid interfacial curvature and surfactant formulation [41]. The magnitude of gas viscosity is 1.66e-5 Pa-s and α is a function of gas fractional flow as described in ref. [19]. Hence, we obtained a comparison of the apparent viscosity of foam in the fracture and the results of an established model. Thereafter, we compared the foam viscosity for gas veloc-
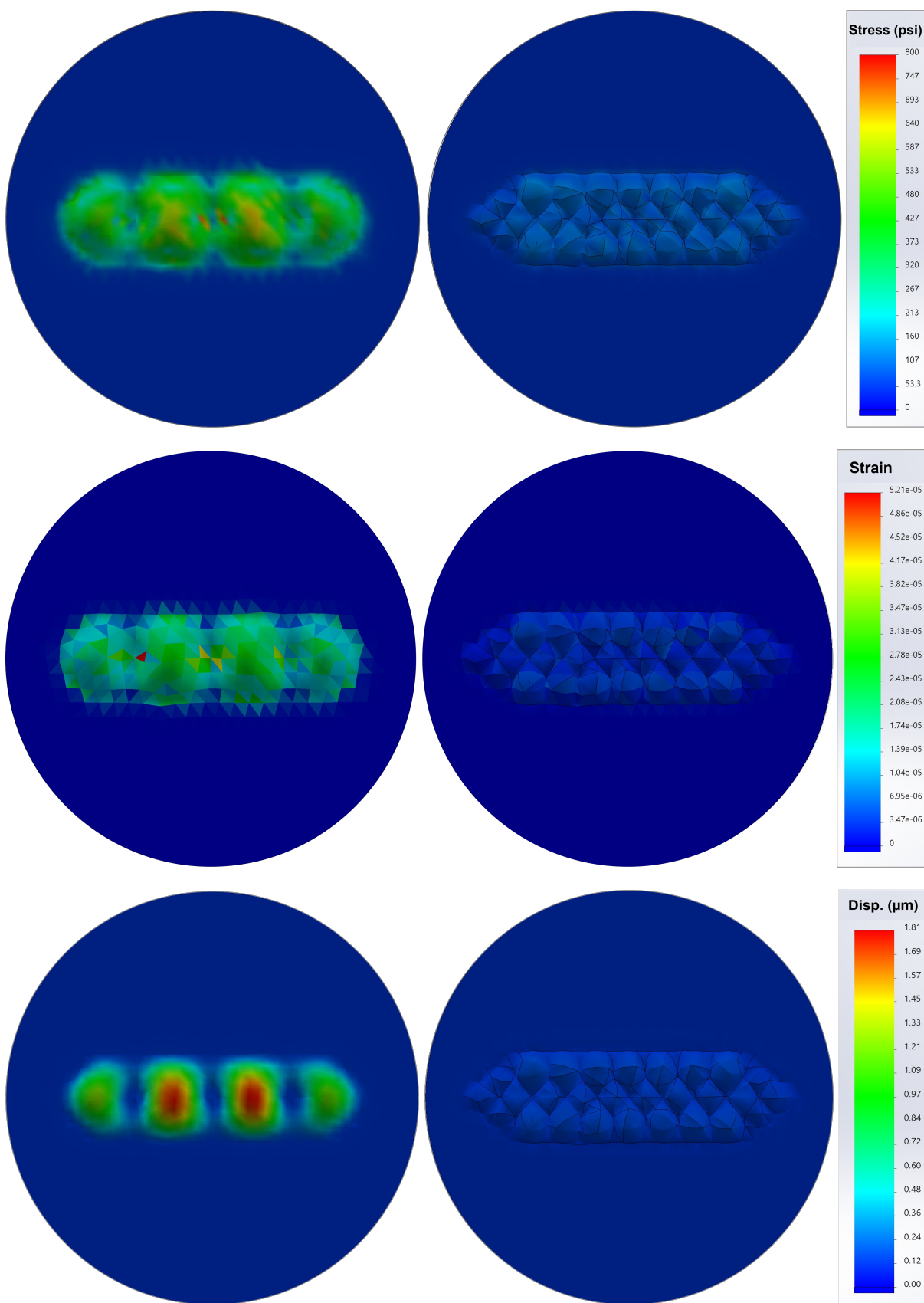
Fig. 4 Stress, strain, and displacement distributions (top to bottom) for 138 kPa hydrostatic pressure for the initial and final designs; Left: the initial micromodel design. Right: the final micromodel design. Notice that results are plotted on a common scale for each quantity.

ity of 11.6 m/day and four foam qualities of 30, 50, 70, and 90%. Figure 5 shows the results of this comparison. The measured error between the experimental model and the numerical study is less than 8%.
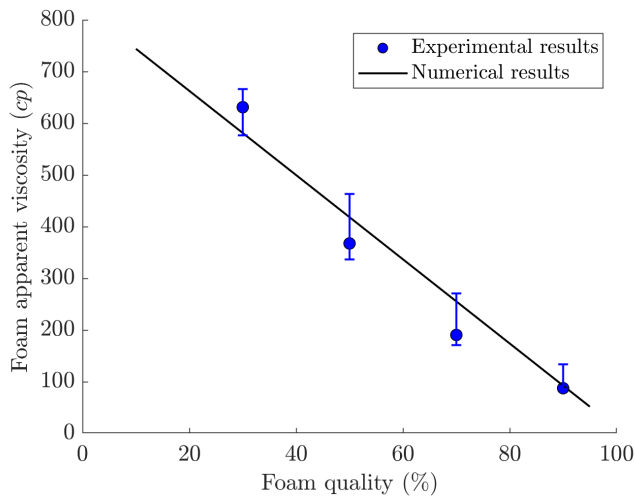

Fig. 5 Validation exercise. Viscosity comparison between experimental results and numerical model. The gas velocity is 11.6 m/day.

5.3 Experiments

Following validation a full range of foam behavior was explored. Table 2 lists the absolute back pressure applied and the associated gas velocity at back pressure. We adjusted water velocity accordingly to generate various foam qualities ranging from 20 to 99%.

Table 2 Flow information for different qualities of injected foam.

Experiment Set #	Absolute back pressure (kPa)	u_g (m/Day)
1	135.83	29.2
2	170.30	23.3
3	204.77	19.4
4	239.25	16.6
5	273.72	14.5
6	308.20	12.9
7	342.67	11.6

Figure 6 shows bubble texture at foam qualities from 20 to 99% for gas velocity of 11.6 m/day. The bubble size increases with increasing foam quality. Additionally, the roundness and smoothness of the bubbles shows a decreasing trend as foam quality increases. That is, polyhedral bubble shapes emerge as quality increases.

Figure 7 shows the cumulative distribution function of bubble areas for two sets of gas velocities: 11.6 m/day and 23.3 m/day. The plots show that bubble size variation is the largest for very dry foam (99% quality) and it decreases with decreasing foam quality. Low quality foam from 20-50% showed small uniform dispersed bubbles in liquid. Image analysis showed that bubbles in this range consisted roughly of 90% small uniform bubbles and 10% of larger and more elongated bubbles. By increasing foam quality, the liquid volume space was reduced and lenses became
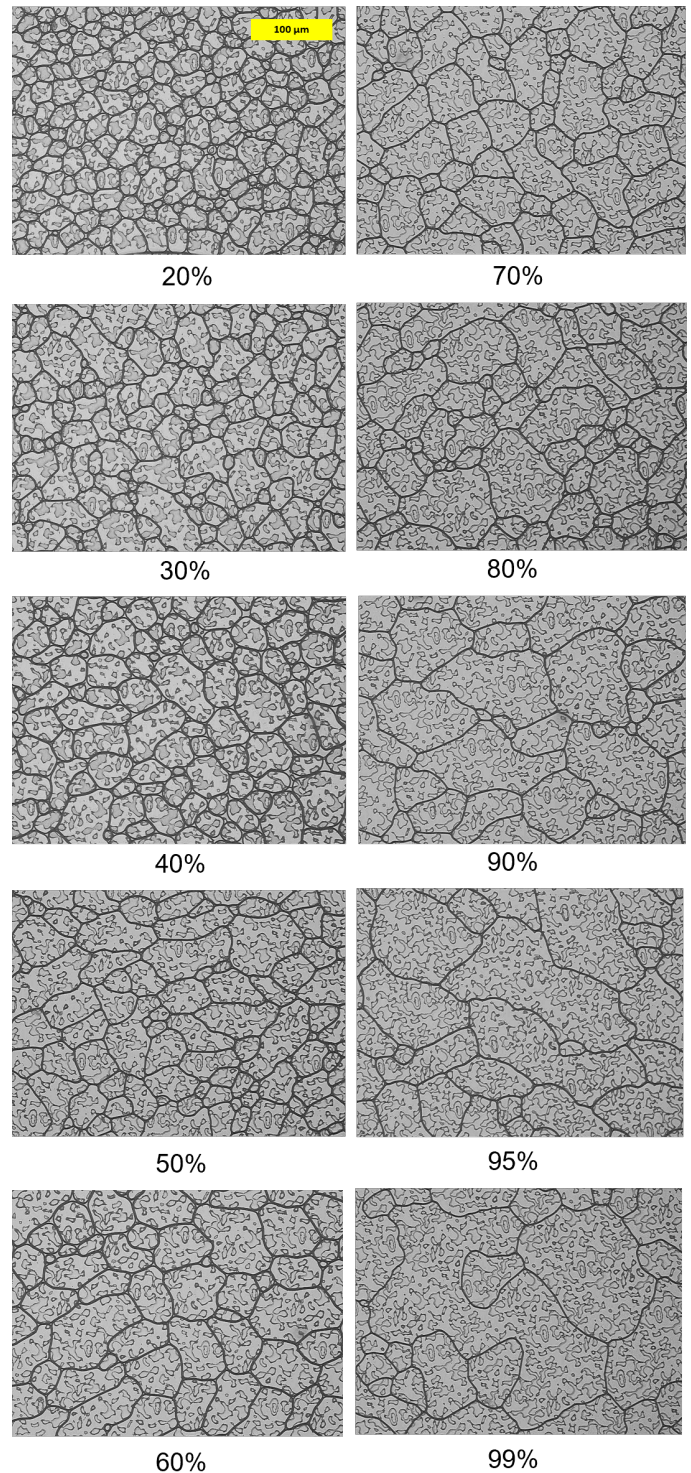

Fig. 6 Examples of the bubble texture along the fracture length at various qualities for gas velocity of 11.6 m/day. The length of the scale bar on the first figure is 100 μm.

thinner. At qualities of 95% and greater, only lamella separate the gas bubbles.

Figure 8 shows pressure gradient versus water velocity for various gas velocities. The pressure gradient is a function of water velocity at small rates of injection up to about 10 m/day. This de-
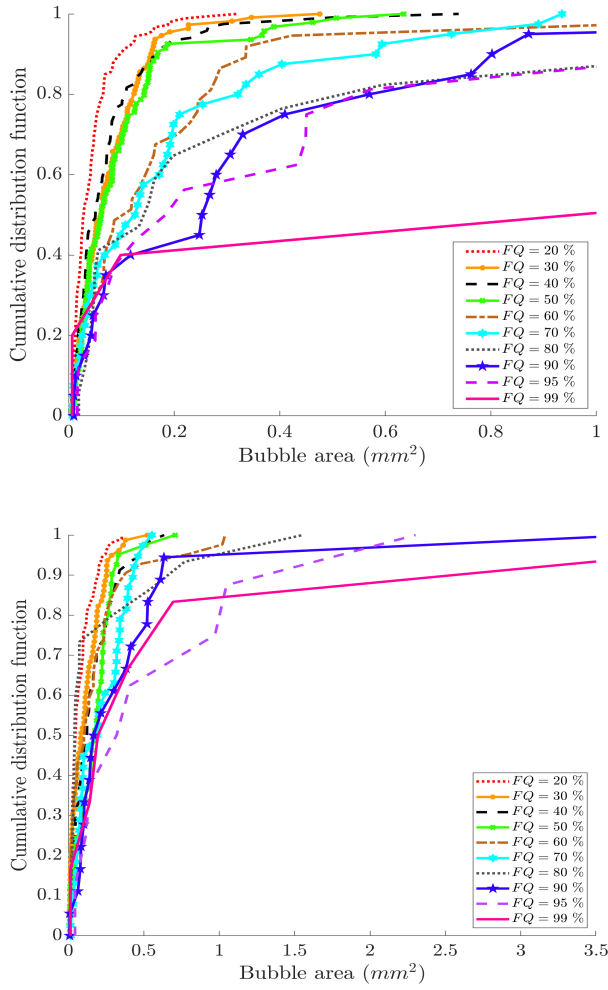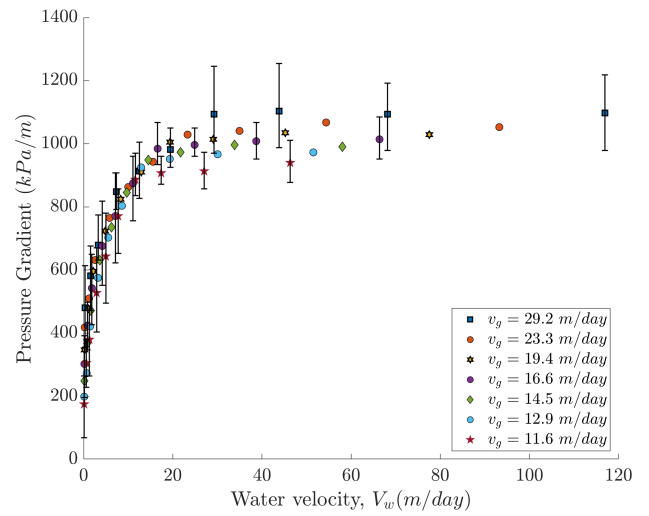
Fig. 8 Pressure drop versus water velocity for the plain fracture at various constant gas velocities. The error bars in the data reflect oscillations in pressure gradient.

Table 3 The fitted parameters for the exponential curve fitted to foam apparent viscosity versus foam quality data for different qualities of injected foam.

u_g (m/Day)	c	b
29.2	776.4	-0.025
23.3	787.8	-0.025
19.4	906.6	-0.025
16.6	1019.0	-0.025
14.5	1038.0	-0.025
12.9	1076.0	-0.025
11.6	1179.0	-0.025

Fig. 7 The cumulative distribution function versus bubble area for gas velocities of 11.6 (top) and 23.3 (bottom) m/day as a function of quality.

pendency lessens at larger rates and pressure gradient gradually becomes independent of water velocity. Additionally, the trends of pressure gradient with different gas velocities show that pressure drop increases with increasing gas velocity. A similar trend was reported by other researchers [7,15]. Pressure gradient decreases by increasing the foam quality. This is in agreement with Kahrobaei et al. [42]. Panchareon et al. [7], AlQuaimi and Rossen [21], and Buchgraber et al. [15] observed similar trends.

Figure 9 shows foam apparent viscosity versus foam quality for more than 50 experimental cases. The viscosity is computed via Eq. 9. An exponential curve in Eq. 11 was fitted to the results as

$$\mu_f = c \, exp(bQ_f) \tag{11}$$

Table 3 lists the parameters for the exponential curve fitted to foam apparent viscosity versus foam quality data for different qualities of injected foam. By bounding the value of b, the coefficient c increases as gas velocity decreases. Additionally, comparing all the cases reveals that foam apparent viscosity is a strong function of foam quality for small qualities. However, this dependency decreases for larger foam qualities.
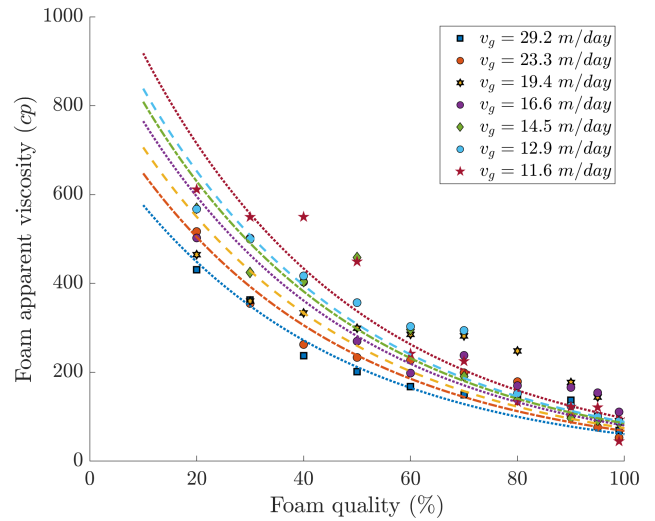

Fig. 9 Foam apparent viscosity versus foam quality for different qualities of injected foam. Dotted lines are correlation.

Figure 10 reveals the complex interplay of foam texture and flow rate on foam rheology that is measurable using the new foam rheometer. The figure shows foam viscosity calculated using equation Eq. 9 versus the observed $n_f/v_f^{1/3}$ for different constant

rates of injected gas. For each constant gas flow rate, we covered foam qualities of 20 to 99% with quality increasing from left to right. At foam qualities beginning from 20% and up to 50–60%, foam bubble size at a given flow rate does not change remarkably, as shown in Fig. 6. For the smaller qualities, foam bubbles are separated by liquid slugs; the radius of curvature is constant and smaller or equal to the fracture aperture[41]. Accordingly, shear thinning apparent viscosity is evident in the lower quality region. That is, the viscosity increases as $v_f^{-1/3}$ increases (i.e., quality increases at a fixed gas rate).

The local maximum in apparent viscosity for each gas velocity occurs at qualities ranging from about 70 to 90%. As the quality increases and the foam becomes drier, bubbles become more polyhedral and capillary suction of foam lamellae increases. Coalescence coarsens the foam and decreases n_f substantially. For instance, bubble sizes more than double between 70% and 99% quality in Fig. 5. Hence, effective viscosity decreases to the right of the local maximum because n_f drops sharply. Taken all together, Fig. 10 teaches that there is a foam quality that maximizes apparent viscosity during flow in fractures and that this optimal quality has a slight gas rate dependence.
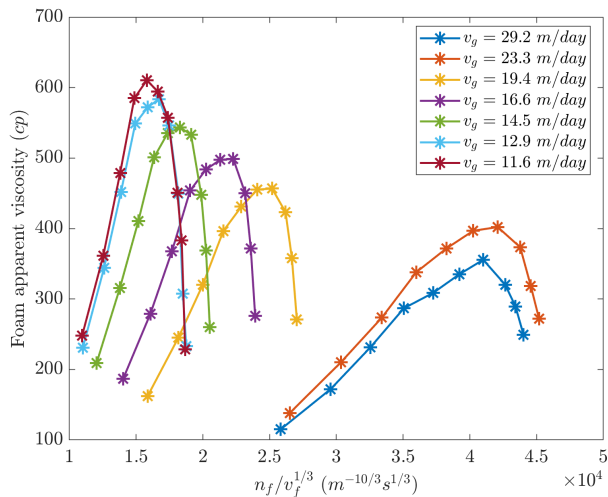

Fig. 10 Foam viscosity calculated using equation Eq. 9 versus $n_f/v_f^{1/3}$ for different rates of injected gas. Each plot covers foam qualities of 20 to 99%, starting from the left side of the plot. Lines connect data points to guide the eyes.

6 Concluding Remarks

This paper describes the development and creation of a novel microfluidic rheometer to study foam behavior in planar fractures. This device is a 7-cm by 2-cm (see Figure 1) fracture with a 25 μm aperture incorporating roughness that is etched onto a silicon wafer. Importantly, the rheometer permits direct observation of foam bubble shape, average size, and size distribution that vary with liquid and gas velocities.

We conducted more than 50 experiments to probe and explain foam flow properties in a planar fracture. This unique design enables rapid quantification of the cumulative distribution function of bubble area. It shows that the maximum bubble size increases

and becomes more variable for very dry foam. The bubble-size distribution also reveals that low quality foam ranging from 20 to 50% by volume gas contains sparsely dispersed bubbles in liquid. The bubbles consist roughly of 90% small uniform bubbles and only 10% of larger and more elongated bubbles. This observation is in agreement with the findings of[15]; however, after extensive investigation, we narrowed the range from 20-70% to 20-50%.

The pressure drop versus liquid velocity plot illustrates the dependency of pressure gradient on water phase velocity for small rates of injection up to 10 m/day. Additionally, our results show that by increasing the gas velocity, the pressure gradient increases. Analyzing apparent viscosity for different foam qualities and various water velocities shows that foam apparent viscosity is a strong function of water velocity when foam quality is large, but this dependency decreases for wetter, lower-quality foams. For the wettest foams, the pressure drop is independent of liquid velocity at a given gas velocity. On the other hand, high quality foams are sensibly independent of gas flow rate, at a given liquid velocity.

Conflicts of interest

The authors declare that they have no known competing financial interests or personal relationships that could have appeared to influence the work reported in this paper.

Acknowledgements

Nomenclature

$[B]$	displacement differentiation matrix
$[E]$	elasticity matrix
$[k]$	stiffness matrix
$[N]$	matrix of shape function
α	flow resistance factor
ε	strain
ε^t	thermal part of strain
λ	elastic lame constant 1
μ	elastic lame constant 2
μ_{app}	foam apparent viscosity
μ_g	gas viscosity
ν	Poisson ratio
σ	stress

$\{h\}$	thermal vector
$\{p\}$	force vector from volume and surface loads
$\{p^S\}$	vector of surface force
$\{p^V\}$	vector of body force
$\{q\}$	nodal displacements vector
b	fracture aperture
E	Young's modulus
L	fracture length
P	pressure
Q_f	foam quality
T	temperature
u_g	gas velocity
v_f	foam velocity normalized by foam quality
v_w	water velocity
f	load vector

Notes and references

1 D. Lord, *Journal of Petroleum Technology*, 1981, **33**, 39–45.

2 D. H. Smith, *Energy & Fuels*, 1996, **10**, 266–266.

3 D. Langevin, *Chemphyschem : a European journal of chemical physics and physical chemistry*, 2008, **9**, 510–22.

4 Øyvind Eide, M. Fernø, S. Bryant, A. Kovscek and J. Gauteplass, *Journal of Natural Gas Science and Engineering*, 2020, **80**, 103378.

5 G. G. Bernard and L. W. Holm, *Society of Petroleum Engineers Journal*, 1964, **4**, 267–274.

6 L. W. Holm, *Society of Petroleum Engineers Journal*, 1968, **8**, 359–369.

7 M. Pancharoen, M. A. Fernø and A. R. Kovscek, *Journal of Petroleum Science and Engineering*, 2012, **100**, 50–58.

8 N. Nazari, J.-S. Tsau and R. Barati, *Energies*, 2017, **10**, 516.

9 W. R. Rossen, *Foams*, Routledge, 2017, pp. 413–464.

10 R. Barati, N. Nazari, J.-S. Tsau and E. Peltier, ABSTRACTS OF PAPERS OF THE AMERICAN CHEMICAL SOCIETY, 2017.

11 C. Conn, K. Ma, G. Hirasaki and S. Biswal, *Lab on a chip*, 2014, **14**,.

12 M. M. Almajid, N. Nazari and A. R. Kovscek, *Energy & Fuels*, 2019, **33**, 11353–11363.

13 C.-Y. Lai, B. Rallabandi, A. Perazzo, Z. Zheng, S. Smiddy and H. Stone, *Proceedings of the National Academy of Sciences*, 2018, **115**,.

14 H. Bertin, O. Apaydin, L. Castanier and A. Kovscek, *SPE Journal*, 1999, **4**, 75–82.

15 M. Buchgraber, L. M. Castanier and A. R. Kovscek, SPE Annual Technical Conference and Exhibition, 2012.

16 R. Farajzadeh, B. Wassing and P. Boerrigter, SPE Annual Technical Conference and Exhibition, 2010.

17 A. Kovscek, D. Tretheway, P. Persoff and C. Radke, *Journal of Petroleum Science and Engineering*, 1995, **13**, 75–86.

18 J. Gauteplass, K. Chaudhary, A. R. Kovscek and M. A. Fernø, *Colloids and Surfaces A: Physicochemical and Engineering Aspects*, 2015, **468**, 184–192.

19 N. Nazari, M. M. Almajid and A. R. Kovscek, *Advances in Water Resources*, 2022, **162**, 104154.

20 W. Yan, C. A. Miller and G. J. Hirasaki, *Colloids and Surfaces A: Physicochemical and Engineering Aspects*, 2006, **282-283**, 348–359.

21 B. I. AlQuaimi and W. R. Rossen, *Energy & Fuels*, 2019, **33**, 68–80.

22 M. A. Fernø, J. Gauteplass, M. Pancharoen, A. Haugen, A. Graue, A. R. Kovscek and G. Hirasaki, *SPE journal*, 2016, **21**, 1140–1150.

23 Z. Xu, A. Cao, L. Chen, S. Cui, G. Yu and Z. Li, *Industrial & Engineering Chemistry Research*, 2020, **59**, 19817–19828.

24 L. Chen, M. Huang, Z. Li, D. Liu and B. Li, *Journal of Petroleum Science and Engineering*, 2020, **185**, 106663.

25 M. J. Shojaei, A. Rodríguez de Castro, Y. Méheust and N. Shokri, *Journal of Colloid and Interface Science*, 2019, **552**, 464–475.

26 M. R. Islam, A. Chakma, T. A. MacDonald and S. M. Farouq Ali, AIChE Symposium Series, 1991, pp. 74–88.

27 R. Ettinger and C. Radke, *SPE Reservoir Engineering*, 1992, **7**, 83–90.

28 N. Nazari, J.-S. Tsau and R. Barati, SPE Improved Oil Recovery Conference, 2018.

29 N. Nazari, H. Hosseini, J. S. Tsau, K. Shafer-Peltier, C. Marshall, Q. Ye and R. B. Ghafarokhi, *Fuel*, 2020, **261**, 116360.

30 H. Princen, *Journal of Colloid and Interface Science*, 1983, **91**, 160–175.

31 A. R. Kovscek and C. J. Radke, in *Fundamentals of Foam Transport in Porous Media*, ch. 3, pp. 115–163.

32 K. Li, K.-H. A. A. Wolf and W. R. Rossen, *Transport in Porous Media*, 2021, **138**, 185–200.

33 S. Gupta, W. S. Wang and S. A. Vanapalli, *Biomicrofluidics*, 2016, **10**, 043402.

34 S. Haward, *Biomicrofluidics*, 2016, **10**, 043401.

35 F. Del Giudice, *Micromachines*, 2022, **13**, 167.

36 W. Yun, C. Ross, S. Roman and A. Kovscek, *Lab Chip*, 2017, **17**, 1462–1474.

37 S. Aldousary and A. R. Kovscek, *Journal of Petroleum Science and Engineering*, 2019, **179**, 606–614.

38 G. P. Nikishkov, 2004, 1–31.

39 M. Buchgraber, M. Al-Dossary, C. Ross and A. Kovscek, *Journal of Petroleum Science and Engineering*, 2012, **86-87**, 27–38.

40 W. Yun and A. R. Kovscek, *Journal of Petroleum Science and Engineering*, 2015, **128**, 115–127.

41 G. J. Hirasaki and J. B. Lawson, *SPE Journal*, 1985, **25**, 176–190.

42 S. Kahrobaei, S. Vincent-Bonnieu and R. Farajzadeh, *Scientific Reports*, 2017, **7**,.